

# Bimetallic nanoalloys planted on super-hydrophilic carbon nanocages featuring tip-intensified hydrogen evolution electrocatalysis

Received: 8 March 2024

Accepted: 5 August 2024

Published online: 21 August 2024



Linjie Zhang<sup>1,7</sup>, Haihui Hu<sup>1,7</sup>, Chen Sun<sup>1</sup>, Dongdong Xiao<sup>2</sup>, Hsiao-Tsu Wang<sup>3</sup>, Yi Xiao<sup>1</sup>, Shuwen Zhao<sup>1</sup>, Kuan Hung Chen<sup>4</sup>, Wei-Xuan Lin<sup>4</sup>, Yu-Cheng Shao<sup>5</sup>, Xiuyun Wang<sup>6</sup>, Chih-Wen Pao<sup>5</sup> & Lili Han<sup>1</sup>✉

The insufficient availability and activity of interfacial water remain a major challenge for alkaline hydrogen evolution reaction (HER). Here, we propose an “on-site disruption and near-site compensation” strategy to reform the interfacial water hydrogen bonding network via deliberate cation penetration and catalyst support engineering. This concept is validated using tip-like bimetallic RuNi nanoalloys planted on super-hydrophilic and high-curvature carbon nanocages (RuNi/NC). Theoretical simulations suggest that tip-induced localized concentration of hydrated  $K^+$  facilitates optimization of interfacial water dynamics and intermediate adsorption. In situ synchrotron X-ray spectroscopy endorses an  $H^*$  spillover-bridged Volmer–Tafel mechanism synergistically relayed between Ru and Ni. Consequently, RuNi/NC exhibits low overpotential of 12 mV and high durability of 1600 h at 10 mA cm<sup>-2</sup> for alkaline HER, and demonstrates high performance in both water electrolysis and chlor-alkali electrolysis. This strategy offers a microscopic perspective on catalyst design for manipulation of the local interfacial water structure toward enhanced HER kinetics.

Hydrogen ( $H_2$ ) is an increasingly important piece of the net zero emissions by 2050 puzzle<sup>1–3</sup>. So far, the most promising route for sustainable green  $H_2$  production is the alkaline water electrolysis powered by renewable electricity<sup>4</sup>. Unfortunately, its commercial implementation is frustrated by the sluggish water dissociation ( $H_2O + * + e^- \rightarrow H^* + OH^-$ ) kinetics of the cathodic hydrogen evolution reaction (HER)<sup>5,6</sup>. In this context, considerable interest has been given to leveraging the adsorption energies of  $H^*$  and  $OH^*$  intermediates in line with the bifunctional mechanism<sup>7</sup>. Consequently, versatile transition-

metal alloy catalysts exhibiting dual-site synergy have been developed<sup>8,9</sup>. Despite remarkable progress, the intrinsic site-specific kinetics of these alloys typically fall short of that exhibited by noble Pt, the current state-of-the-art HER catalyst. Additionally, their vulnerable intermetallic synergy during prolonged catalysis remains an unresolved concern<sup>10</sup>. This underscores that, to underpin the success of catalyst synthesis, it is crucial to not only consider the electronic regulation achieved through alloying but also to meticulously tailor the local interfacial structure.

<sup>1</sup>State Key Laboratory of Structural Chemistry, Fujian Institute of Research on the Structure of Matter, Chinese Academy of Sciences, Fuzhou 350002, China.

<sup>2</sup>Beijing National Laboratory for Condensed Matter Physics, Institute of Physics, Chinese Academy of Sciences, Beijing 100190, China. <sup>3</sup>Bachelors's Program in Advanced Materials Science, Tamkang University, New Taipei City 251301, Taiwan. <sup>4</sup>Department of Physics, Tamkang University, New Taipei City 25137, Taiwan. <sup>5</sup>National Synchrotron Radiation Research Center, Hsinchu 300092, Taiwan. <sup>6</sup>National Engineering Research Center of Chemical Fertilizer Catalyst, Fuzhou University, Fuzhou 350002, China. <sup>7</sup>These authors contributed equally: Linjie Zhang, Haihui Hu. ✉e-mail: [llhan@fjirsm.ac.cn](mailto:llhan@fjirsm.ac.cn)

Virtually, besides water dissociation, the interfacial water availability and activity are also two pivotal factors determining the alkaline HER activity but have received relatively less attention<sup>11,12</sup>. Recent studies have shown that the hydrogen bonding network connectivity of near-surface water molecules in the electric double layer (EDL) plays a key role in addressing the water supply issues in alkaline HER, highlighting the importance of OH\* favorably adsorbed on the catalyst surface<sup>13–16</sup>. Although these findings fundamentally clarify the kinetic hysteresis in alkaline HER, they fail to explain the yet unsatisfactory HER activity of those alloy catalysts that comprise metal with a high OH\* affinity<sup>17</sup>. Indeed, it is generally neglected that, in high pH electrolytes, an increased degree of hydrogen bonding tends to form a rigid, ice-like interfacial water layer. This layer may not only deactivate the O–H stretch for water dissociation but also impedes the diffusion of dissociated OH<sup>−</sup> across the EDL to the bulk solution, thus hindering active site recovery<sup>18–20</sup>. Moreover, the OH<sup>−</sup> adsorbed on catalyst surface can stabilize the dissociated OH\* via hydrogen bonding interactions, making their desorption more difficult<sup>21</sup>. These concomitant side-effects are believed to compromise the HER performance due to the presence of a robust interfacial hydrogen bonding network. Therefore, it is essential to find a way out of this dilemma to unlock the full potential of catalysts for alkaline HER. The formulation of a viable strategy to customize the interfacial structure, thereby facilitating an engineered hydrogen bonding network within the EDL, is highly sought after.

In this study, we introduce an “on-site disruption and near-site compensation” strategy designed to reshape the hydrogen bonding network, thus achieving a trade-off between water availability and activity at the catalyst interface (Supplementary Fig. 1). To demonstrate this concept, we elaborately architect a range of Ni-based bimetallic nanoalloys planted on super-hydrophilic N-doped carbon nanocages (MNi/NC, where M denotes the other metals Ru, Pt, Pd, Cu, Zn in each individual alloy) via an intriguing “Kirkendall hollowing and alloying” process. The nanoalloys act as nanotips protruding from the carbon nanocages, featuring the “tip effect” which induces tip-enhanced local electric field, thereby concentrating hydrated electrolyte cations on their surfaces<sup>22,23</sup>. This configuration is supposed to significantly disrupt the hydrogen bonding network within the EDL, thus increasing its flexibility and altering the OH\* binding strength, which facilitates the OH\* intermediates removal into the bulk<sup>24–26</sup>. In addition, the penetration of hydrated cations can transport polarized water molecules to the catalyst surface in an H-down orientation, thus augmenting the kinetics of water dissociation<sup>11,27–30</sup>. Moreover, the super-hydrophilic character of the carbon nanocages support, endowed by the abundant surface OH functional groups, is expected to compensate for the integrality of hydrogen bonding network spatially adjacent to the EDL, thereby counteracting the perturbations caused by intruding cations. By leveraging this reorganized interfacial hydrogen bonding network, the exemplary RuNi/NC catalyst features tip-intensified alkaline HER activity with both low overpotential of 12 mV at 10 mA cm<sup>−2</sup> and Tafel slope of 30.9 mV dec<sup>−1</sup>, outperforming the established Pt/C benchmark with a 13.6-fold increase in mass activity (5.32 A mg<sub>Ru+Ni</sub><sup>−1</sup> vs. 0.39 A mg<sub>Pt</sub><sup>−1</sup>) at −0.05 V vs. RHE. Furthermore, RuNi/NC displays a strong stability up to 1600 h at 10 mA cm<sup>−2</sup>, ranking it among the leading HER catalysts in alkaline media. Its high HER performance also promises the successes in both practical water electrolysis and chlor-alkali electrolysis, achieving low voltages of 1.42 V and 1.96 V at 10 mA cm<sup>−2</sup>, respectively. Finally, mechanistic insights critically important to the tip-intensified HER activity of RuNi/NC are depicted from both theoretical and in situ studies, revealing significantly ameliorated intermediate binding by the interfacial K<sup>+</sup> cations, and a Ru–Ni dual-site synergy relayed in a hydrogen (H\*) spillover-bridged Volmer–Tafel mechanism.

## Results

### Synthesis and characterizations of MNi/NC

The bespoke MNi/NC catalysts series, including RuNi/NC, PtNi/NC, PdNi/NC, CuNi/NC and ZnNi/NC, were readily synthesized using a generalized method involving tandem high-temperature pyrolysis and “inside-out” Kirkendall alloying and hollowing process (Fig. 1a). Initially, nickel nitrate was coordinated with ethylenediaminetetraacetic acid (H<sub>4</sub>EDTA) to produce the coordination complex [Ni<sub>2</sub>(EDTA)]<sub>n</sub> precursor. Subsequent pyrolysis at 1000 °C in an Ar atmosphere, followed by an acid wash, yielded the intermediary Ni nanoparticles encapsulated in N-doped nanocarbons (Ni@NC). Whereafter, Ni@NC was mixed with specific metal salts and co-annealed in a 5 wt% H<sub>2</sub>-Ar atmosphere at a designated temperature to produce the final MNi/NC catalyst. Notably, during the conversion from Ni@NC to MNi/NC, the bulk of encapsulated Ni nanoparticles migrated outward and reacted with the other metal present on the surface, forming smaller-sized nanoalloys. This process resulted in a hollow interior and abundant pore channels within the carbon nanocage. This unique structural evolution can be reasoned to the intermingling of metals driven by the typical Kirkendall effect, which arises from the relatively faster diffusion rate of Ni atoms than the targeted metal (M) atoms at elevated temperatures<sup>31</sup>. This culminates in a net outward flow of Ni atoms toward the surface, and the subsequent vacancies coalesce into the Kirkendall voids at the original sites of the Ni nanoparticles.

Transmission electron microscope (TEM) analysis of the intermediary Ni@NC reveals the presence of buried Ni nanoparticles with an average size of ca. 10 nm within the onion-like multilayered graphitic nanocarbons (Fig. 1b, c and Supplementary Fig. 2). In contrast, TEM images of MNi/NC clearly illustrate the formation of hollow carbon nanocages, characterized by shell thicknesses ranging from 2 to 3 nm and diameters spanning 5–10 nm, with curvature radii varying from 2.1 to 6.0 nm (Supplementary Fig. 3). The external surfaces of the nanocages are intricately adorned with Ni-based bimetallic nanoalloys resembling nanotips protruding from the high-curvature carbon nanocages. High-angle annular dark field (HAADF) scanning transmission electron microscopy (STEM) mapping exhibits the evenly distributed bimetallic elements within these nanoalloys (Fig. 1d–m and Supplementary Figs. 4–8). And atomic-resolution HAADF imaging using aberration-corrected STEM (AC-STEM) reveals well-matched lattice atomic arrangements corresponding to Ru<sub>1.68</sub>Ni<sub>0.32</sub> (hexagonal), PtNi<sub>3</sub> (cubic), Pd<sub>0.19</sub>Ni<sub>0.81</sub> (cubic) and CuNi<sub>3</sub> (cubic) and Zn<sub>0.08</sub>Ni<sub>0.92</sub> (cubic), respectively. Furthermore, their metal contents determined by inductively coupled plasma-atomic emission spectrometry (ICP–AES) are presented in Supplementary Table 1. As observed, a discrepancy in the alloy composition is evident for these MNi/NC samples, especially for RuNi/NC, which exhibits a much lower Ni content. This disparity might be attributed to the significant lattice mismatch between hexagonal Ru and cubic Ni, which likely impedes the complete Kirkendall alloying process, resulting in some Ni nanoparticles remaining unalloyed within the graphitic carbon nanocages. Various factors, such as lattice matching, atomic radius, electronic configuration, and thermodynamic compatibility of the metals are posited to collectively influence the kinetics of Kirkendall alloying, and consequently determine the final alloy structure.

The definitive phase structures of these nanoalloys were corroborated through X-ray diffraction (XRD) analysis (Fig. 1n). Except for RuNi/NC, which shows diffraction peaks corresponding to hexagonal Ru<sub>1.68</sub>Ni<sub>0.32</sub> and residual cubic Ni, all other MNi/NC samples exhibit similar patterns to Ni@NC and match well with the standard patterns of their respective cubic alloy structures. Notably, a comparison between Ni@NC and the MNi/NC series reveals a significant attenuation of the graphite (002) peak at 26° in the latter, accompanied by the emergence of an amorphous carbon peak at a lower angle. This observation indicates an impaired graphite structure and evidences the Kirkendall alloying process during which intermetallic

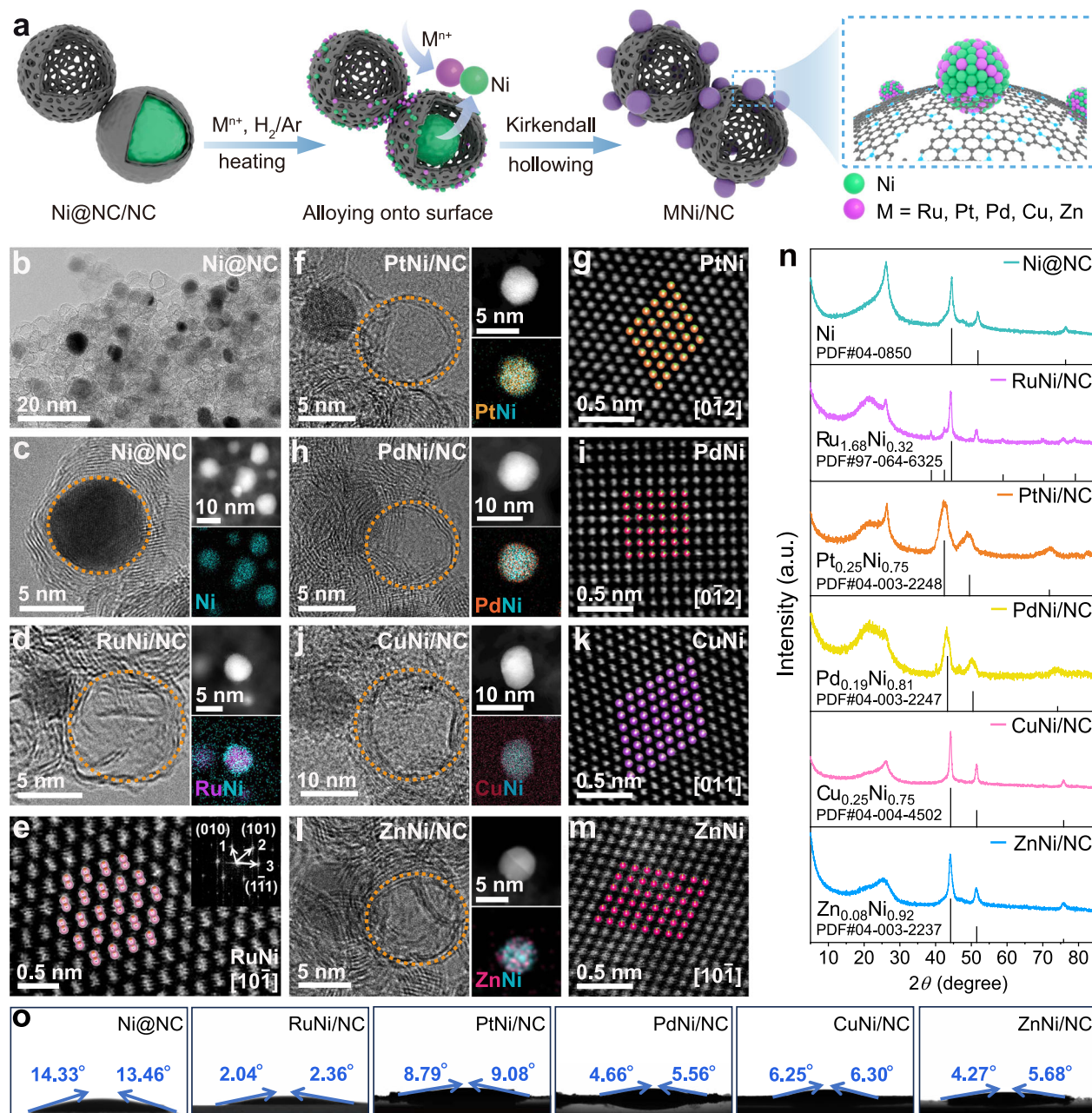


**Fig. 1 | Schematic synthesis and structural characterizations of MNi/NC (M = Ru, Pt, Pd, Cu, Zn) catalysts.** **a** Schematic illustration of the synthetic process of MNi/NC. **b, c** TEM images of Ni@NC. **d-m** HAADF-STEM images (the orange dashed circles sketch the outlines of the curved carbon nanocages) and EDS

mappings of MNi/NC, and AC-STEM images of MNi nanoalloys (insets are the schematic crystallographic atomic arrangements): (d, e) RuNi/NC; (f, g) PtNi/NC; (h, i) PdNi/NC; (j, k) CuNi/NC; (l, m) ZnNi/NC. **n** XRD patterns of Ni@NC and MNi/NC. **o** Optical images showing water contact angles of Ni@NC and MNi/NC series.

interdiffusion across the carbon layers occurred. Such Kirkendall alloying is anticipated to engender a strong metal-support interaction that not only upgrades the electronic structures of nanoalloys but also establishes a robust linkage between the nanoalloy and carbon nanocages conducive to sustained electrocatalysis. Besides, after Kirkendall alloying, all MNi/NC samples exhibit enhanced water affinity compared to Ni@NC, as evidenced by their super-hydrophilic characters with low water contact angles  $<10^\circ$  (Fig. 1o and Supplementary Fig. 9). The super-hydrophilicity of MNi/NC is primarily attributed to the rich surface oxygen-containing functional groups and defects inherited from Ni@NC formed during the pickling process, and might be further amplified by the increased surface roughness and microporosity resulting from the Kirkendall alloying process. Importantly, this super-hydrophilicity could play a crucial role in enhancing the HER

electrocatalytic activity by endowing the material with improved electrolyte accessibility, enhanced mass transport, increased active site availability, stabilized reaction intermediates, and reduced charge transfer resistance.

### 3D electron tomography and X-ray spectroscopic analysis of RuNi/NC

To meticulously dissect the local microstructural attributes, RuNi/NC was selected as a prototypical example from the MNi/NC series for an in-depth analysis. The STEM image presented in Fig. 2a clearly shows the uniform dispersion of RuNi nanoalloys on carbon nanocages, exhibiting a mean diameter of 2 nm (Supplementary Fig. 10). The well-defined lattice atomic arrangement, characteristic of the hexagonal  $P6_3/mmc$  Ru<sub>1.68</sub>Ni<sub>0.32</sub> alloy oriented along the  $[10\bar{1}]$  zone axis, is



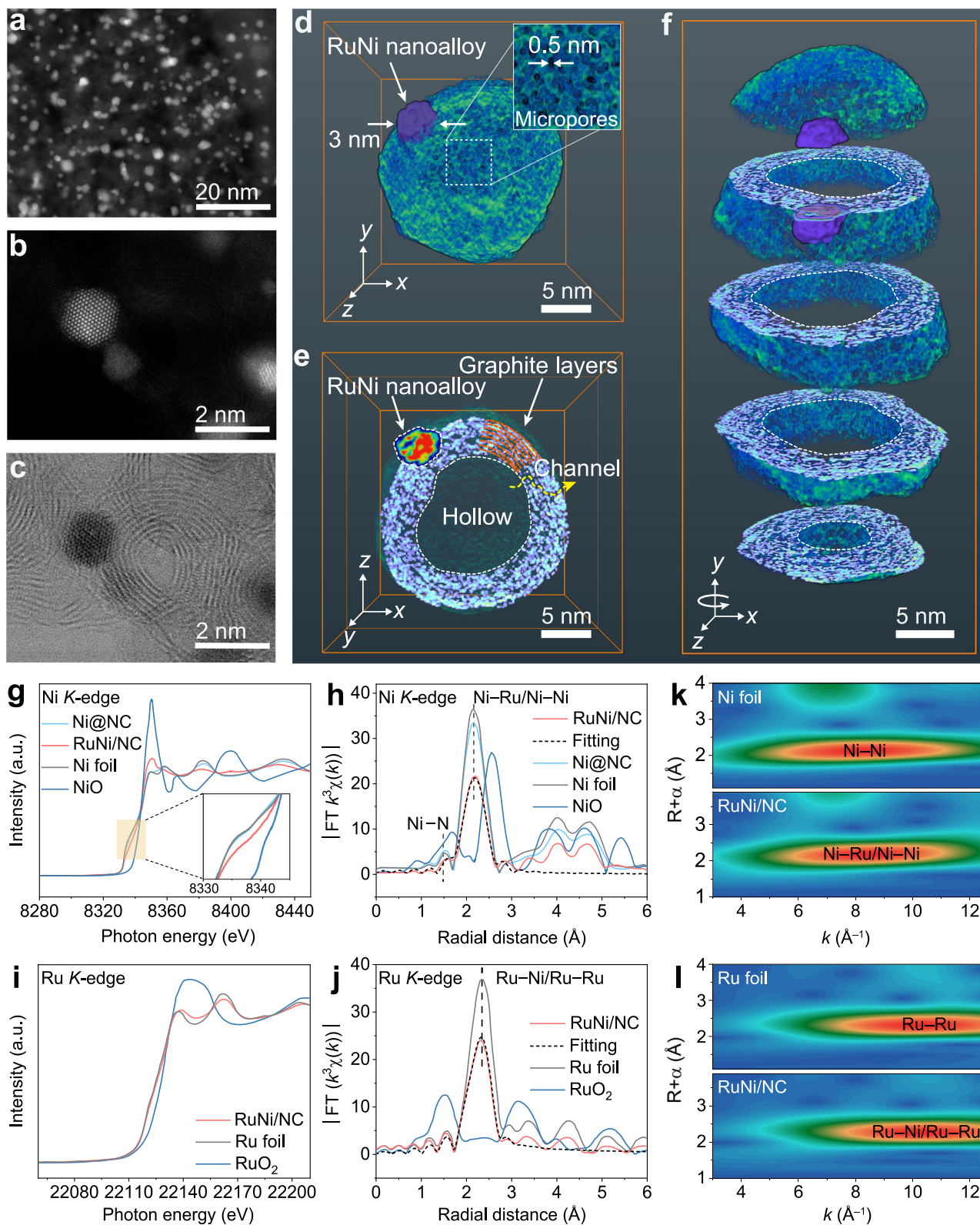


**Fig. 2 | 3D TEM tomography and ex situ synchrotron XAFS study of RuNi/NC.** **a–c** HAADF and AC-STEM images of RuNi/NC. **d** 3D visualization of a single RuNi/NC nanoparticle, showing the partial embedding of RuNi nanoalloy within the carbon nanocage shell, achieved through electron tomography technique. **e** Cross-section of RuNi/NC, highlighting the multilayer porous shell and hollow cavity of

the carbon nanocage. **f** Laminated cross-sections and isosurfaces of RuNi/NC. **g** XANES and **(h)** FT-EXAFS spectra at the Ni K-edge of Ni@NC, RuNi/NC, Ni foil, and NiO. **i** XANES and **(j)** FT-EXAFS spectra at the Ru K-edge of RuNi/NC, Ru foil, and RuO<sub>2</sub>. Wavelet transform analysis of **(k)** Ni K-edge and **(l)** Ru K-edge EXAFS oscillations of RuNi/NC.

distinctly portrayed in Fig. 2b. Furthermore, the annular bright field (ABF) STEM image in Fig. 2c clearly delineates that the RuNi nanoalloy is effectively supported by the carbon nanocages featuring continuous multilayer graphite lattice fringes. To resolve the local structure more comprehensively, we performed three-dimensional (3D) electron tomography for RuNi/NC (Supplementary Movie 1). The 3D structural visualization depicts a singular RuNi nanoalloy about 3 nm in size planted on a carbon nanocage with an approximate diameter of 20 nm, as vividly shown in Fig. 2d and Supplementary Fig. 11. The pony-size carbon nanocage, distinguished by its high-curvature surface, renders the RuNi nanoalloy a nanotip-like protrusion, thus inducing a typical tip effect on the RuNi nanoalloy with a locally enhanced electric field<sup>32</sup>. Additionally, as a result of the outward Kirkendall diffusion of Ni atoms, substantial micropores are observed across the entire structure of the carbon nanocage. This observation is further attested by the high specific surface area ( $326.3 \text{ m}^2 \text{ g}^{-1}$ ) and total pore volume ( $1.18 \text{ cm}^3 \text{ g}^{-1}$ ) of RuNi/NC, as measured by  $\text{N}_2$  isothermal sorption (Supplementary Fig. 12). The cross-section depicted in Fig. 2e unveils the apparent hollow cavity within the carbon nanocage composed of multiple graphite layers. Their graphitic structure is verified by Raman spectra (Supplementary Fig. 13), ensuring a highly conductive network favorable for electrocatalysis<sup>33,34</sup>. Notably, it distinctly discloses that the tip-like RuNi nanoalloy is partially embedded within the shell region of the carbon nanocage. This configuration affirms a robust metal-support interaction, indicative of a promising and enduring framework for electrocatalysis. Such intimate integration between the RuNi nanoalloy and the carbon nanocage is further elucidated by the laminated cross-sections and isosurfaces of RuNi/NC, as depicted in Fig. 2f.

The local electronic structures of Ni and Ru atoms in RuNi/NC were then investigated by X-ray absorption spectroscopy (XAS). Figure 2g illustrates that the X-ray absorption near edge structure (XANES) spectroscopy reveals nearly coincident Ni *K*-edges for Ni@NC and Ni foil, indicating the metallic state of Ni in Ni@NC<sup>35</sup>. Conversely, the Ni *K*-edge of RuNi/NC is situated between those of Ni foil and NiO, exhibiting a more pronounced white line peak compared to Ni@NC. This suggests that the Ni valence in RuNi/NC is intermediate between 0 and +2, likely due to electron transfer from Ni to the more electronegative Ru in the RuNi nanoalloy, a finding that is consistent with the X-ray photoelectron spectroscopy (XPS) analysis (Supplementary Figs. 14–16). The local coordination environment of Ni atoms in RuNi/NC was probed by Fourier transformed extended X-ray absorption fine structure (FT-EXAFS) spectroscopic curve fitting analysis (Supplementary Fig. 17). The Ni *K*-edge EXAFS spectrum shows a prominent peak at  $2.15 \text{ \AA}$ , attributed to Ni–Ru and Ni–Ni bonds, while a fainter peak at  $1.56 \text{ \AA}$  corresponds to the Ni–N bond (Fig. 2h, Supplementary Tables 2 and 3)<sup>36</sup>. Besides, the Ru *K*-edge XANES spectrum of RuNi/NC aligns with that of Ru foil (Fig. 2i), and the Ru *K*-edge EXAFS of RuNi/NC reveals a significant peak at  $2.33 \text{ \AA}$ , indicative of Ru–Ni and Ru–Ru bonds (Fig. 2j and Supplementary Table 4)<sup>37</sup>. The wavelet transformed EXAFS of RuNi/NC further distinguishably demonstrates the local bonding information, prominently featuring a strong peak of Ru–Ni bond (Fig. 2k, l).

### Electrocatalytic HER performance

The HER performance of RuNi/NC was assessed in 1 M KOH solution (pH  $13.74 \pm 0.12$ ) by a three-electrode configuration with a rotating disk electrode (RDE) as the working electrode under ambient conditions. For comparison, Ni@NC, Ru/NC (Supplementary Fig. 18) and commercial 20 wt% Pt/C catalysts were also tested under identical conditions. The linear sweep voltammetry (LSV) curves illustrated in Fig. 3a and Supplementary Fig. 19 demonstrate the high electrocatalytic HER activity of RuNi/NC, achieving a low overpotential ( $\eta$ ) of 12 mV to deliver a current

density of  $10 \text{ mA cm}^{-2}$ . This performance markedly surpasses those of Ni@NC (459 mV), Ru/NC (55 mV) and Pt/C (28 mV), poisoning it among the leading results to date. Additionally, RuNi/NC requires merely –43 and –66 mV to attain the current densities of 50 and  $100 \text{ mA cm}^{-2}$ , respectively. The superior HER activity of RuNi/NC is further validated by a 13.6-fold increase in mass activity ( $5.32 \text{ A mg}_{\text{Ru+Ni}}^{-1}$ , with a mass loading of  $0.01 \text{ mg cm}^{-2}$  for Ru and  $0.03 \text{ mg cm}^{-2}$  for Ru + Ni) compared to that of Pt/C ( $0.39 \text{ A mg}_{\text{Pt}}^{-1}$ , with a mass loading of  $0.05 \text{ mg cm}^{-2}$  for Pt) at –0.05 V vs. RHE (as per this potential scale hereafter) (Supplementary Fig. 20). Given their similar electrochemical active surface area (ECSA) estimated from the double-layer capacitance ( $C_{\text{dl}}$ ) of RuNi/NC ( $14.7 \text{ mF cm}^{-2}$ ) and Pt/C ( $14.5 \text{ mF cm}^{-2}$ ) (Supplementary Fig. 21), this result indicates a substantially enhanced intrinsic activity of RuNi nanoalloy active sites compared to Pt. This conclusion can be supported by the significantly higher ECSA-normalized current density of  $0.44 \text{ mA cm}^{-2}$  for RuNi/NC, compared to the  $0.12 \text{ mA cm}^{-2}$  for Pt/C at –0.1 V (Supplementary Fig. 22). To eliminate the mass loading effect and obtain a clearer idea of the intrinsic activity, the turnover frequency (TOF) is calculated for all catalysts (Supplementary Fig. 23). The results demonstrate that RuNi/NC exhibits a significantly higher TOF value than Pt/C across the whole potential range, achieving a TOF of  $1.70 \text{ s}^{-1}$  at an overpotential of 100 mV, which is nearly double that of Pt/C ( $0.89 \text{ s}^{-1}$ ). The underlying reaction kinetics is analyzed by Tafel plots shown in Fig. 3b, revealing that RuNi/NC possesses a Tafel slope as low as  $30.9 \text{ mV dec}^{-1}$ , significantly superior to Pt/C ( $48.1 \text{ mV dec}^{-1}$ ), indicating a rapid HER kinetic essence of RuNi/NC following the highly desired Volmer–Tafel mechanism<sup>38</sup>. This enhanced reaction rate is further corroborated by electrochemical impedance spectroscopy (EIS) measurements, which confirm the lowest charge transfer resistance of RuNi/NC among the samples (Supplementary Fig. 24). Notably, beyond its high performance in alkaline media, RuNi/NC also demonstrates high HER electrocatalytic activity in  $0.5 \text{ M H}_2\text{SO}_4$  (pH  $0.33 \pm 0.03$ ) and 1 M PBS (pH  $7.02 \pm 0.02$ ) electrolytes (Supplementary Figs. 25–28), with impressively low overpotentials of 40 and 56 mV at  $10 \text{ mA cm}^{-2}$ , respectively (Fig. 3c and Supplementary Table 5). These results endow RuNi/NC a high-performance pH-universal HER electrocatalyst across various application scenarios.

To further examine the durability of RuNi/NC for HER, a chronopotentiometric test was conducted at  $10 \text{ mA cm}^{-2}$  in 1 M KOH. As depicted in Fig. 3d, RuNi/NC exhibits a quite high catalytic stability for up to 1600 h, with a minimal potential fading rate of only  $0.036 \text{ mV per hour}$ , which is significantly lower than the  $0.67 \text{ mV per hour}$  observed for Pt/C over a duration of just 130 h under identical conditions. Additionally, the catalytic stability of RuNi/NC was evaluated at higher current densities ranging from 50 to  $300 \text{ mA cm}^{-2}$ , revealing similarly high stability over durations of 140 – 200 h (Supplementary Fig. 29). Such striking robustness validates the high structural stability and corrosion resistance of RuNi/NC, which can be attributed to its structural superiority, including robust metal-support interaction and finely tailored electronic structures. To ascertain the actual contribution of RuNi nanoalloys for HER electrocatalysis, a poisoning experiment was further implemented using potassium thiocyanide (KSCN) as a probe reagent due to its strong complexation ability to metal atoms<sup>39</sup>. As shown in Supplementary Fig. 30, the introduction of 10 mM KSCN into the electrolyte significantly decreased the HER current density on RuNi/NC and increased the overpotential to 125 mV at  $10 \text{ mA cm}^{-2}$ , implying the inhibition of RuNi active sites by KSCN molecules. This indicates that the superior HER performance is predominantly attributed to the RuNi nanoalloys. Importantly, the high electrocatalytic HER performance of RuNi/NC exceeds that of the majority of previously reported Ru- and Ni-based leading HER electrocatalysts in both overpotential and stability metrics at a current density of  $10 \text{ mA cm}^{-2}$  in 1 M KOH electrolyte (Supplementary Table 6).

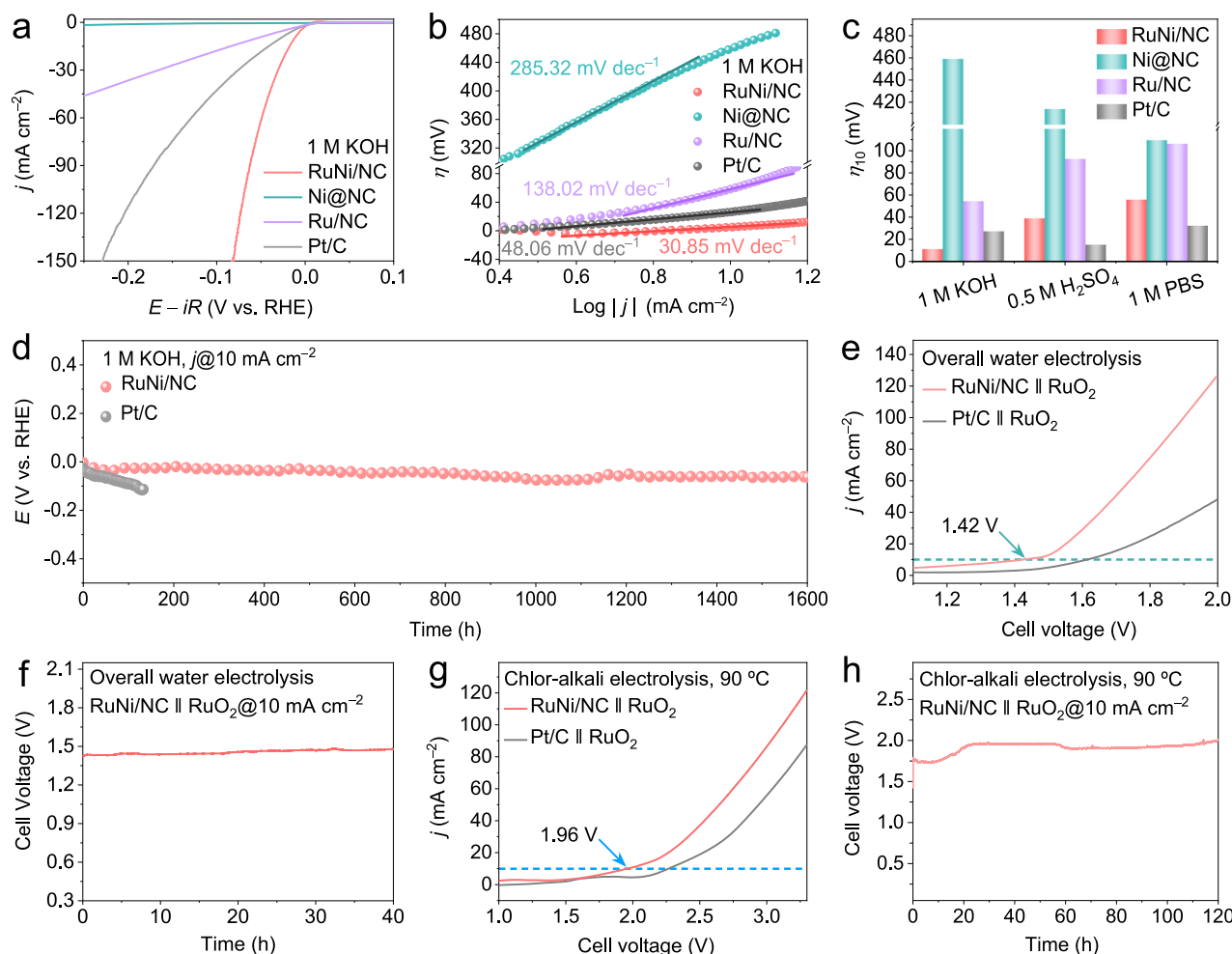


**Fig. 3 | Electrocatalytic HER performances of RuNi/NC.** **a** LSVs in 1 M KOH. **b** Tafel plots in 1 M KOH. **c** Comparison of overpotentials at 10 mA cm<sup>-2</sup> ( $\eta_{10}$ ) in 1 M KOH, 0.5 M H<sub>2</sub>SO<sub>4</sub> and 1 M PBS. **d** Chronoamperometry for stability tests of RuNi/NC and Pt/C at 10 mA cm<sup>-2</sup> in 1 M KOH without *iR*-compensation. The testing conditions include RDE surface area: 0.196 cm<sup>2</sup>, catalyst loading: 0.25 mg cm<sup>-2</sup>, rotation rate: 1600 rpm, scan rate: 5 mV s<sup>-1</sup>, temperature: 25 °C, electrolyte pH: 13.74 ± 0.12 (1 M KOH), 0.33 ± 0.03 (0.5 M H<sub>2</sub>SO<sub>4</sub>), and 7.02 ± 0.02 (1 M PBS), electrolyte resistance: 6.8 ± 0.2 Ω (1 M KOH), 6.2 ± 0.2 Ω (0.5 M H<sub>2</sub>SO<sub>4</sub>), 12.1 ± 0.1 Ω (1 M PBS). **e** LSVs of RuNi/NC || RuO<sub>2</sub> and Pt/C || RuO<sub>2</sub> for overall water electrolysis. **f** Chronopotentiometry of RuNi/NC || RuO<sub>2</sub> for overall water electrolysis at

10 mA cm<sup>-2</sup>. The testing conditions include carbon paper electrode surface area: 1 cm<sup>2</sup>, catalyst loading: 0.25 mg cm<sup>-2</sup>, cell configuration: single cell, scan rate: 5 mV s<sup>-1</sup>, temperature: 25 °C, electrolyte: 1 M KOH (pH 13.74 ± 0.12), and without *iR*-compensation. **g** LSVs of RuNi/NC || RuO<sub>2</sub> and Pt/C || RuO<sub>2</sub> for chlor-alkali electrolysis. **h** Chronopotentiometry of RuNi/NC || RuO<sub>2</sub> for chlor-alkali electrolysis at 10 mA cm<sup>-2</sup>. The testing conditions include electrode surface area: 1 cm<sup>2</sup> (carbon paper or low-carbon steel), catalyst loading: 0.25 mg cm<sup>-2</sup>, cell configuration: H-type cell, membrane: cation exchange membrane, scan rate: 5 mV s<sup>-1</sup>, temperature: 90 °C, electrolytes: saturated NaCl (anolyte, pH 7.01 ± 0.03), and 3 M NaOH and 3 M NaCl (catholyte, pH 14.12 ± 0.11), and without *iR*-compensation.

### Overall water electrolysis and chlor-alkali electrolysis performance

Motivated by the high alkaline HER performance of RuNi/NC, we further explored its practical utility in overall water electrolysis in a 1 M KOH electrolyte, paired with a commercial RuO<sub>2</sub> anode in a single cell. As shown in Fig. 3e, LSVs reveal that the cell necessitates only 1.42 V (without *iR* compensation) to reach a current density of 10 mA cm<sup>-2</sup>, significantly outperforming the Pt/C || RuO<sub>2</sub> electrolyzer (1.61 V), as well as the majority of previously reported Ru-/Ni-based alkaline water electrolysis HER electrocatalysts (Supplementary Table 7). Moreover, the RuNi/NC || RuO<sub>2</sub> electrolyzer demonstrates an impressive capability to sustain a steady current density of 10 mA cm<sup>-2</sup> throughout a prolonged test lasting over 40 h with only minimal voltage decay (Fig. 3f). Notably, during the water electrolysis, drastic bubbling was observed at both the RuNi/NC cathode and RuO<sub>2</sub> anode, while the H<sub>2</sub> bubble flow on RuNi/NC was obviously smoother without any adhesion (Supplementary Fig. 31 and Supplementary Movie 2), highlighting the super-hydrophilic

merit of RuNi/NC surface conducive to the rapid liberation of active sites.

To further assess the practical applicability of RuNi/NC, we conducted experiments mimicking industrial high-temperature (90 °C) chlor-alkali electrolysis conditions. This process simultaneously generates caustic soda, chlorine gas (Cl<sub>2</sub>), and H<sub>2</sub> through brine electrolysis<sup>40,41</sup>. The electrochemical cell consists of two chambers separated by a cation-exchange membrane, with the anode chamber containing a saturated NaCl solution (pH 7.01 ± 0.03) and the cathode chamber filled with a mixture of 3 M NaCl and 3 M NaOH (pH 14.12 ± 0.11) (Supplementary Fig. 32). RuNi/NC was used as the cathode HER catalyst, while commercial RuO<sub>2</sub> was used as the anode catalyst for the chlorine evolution reaction (CIER,  $E^0 = 1.36$  V vs. RHE). As shown in Fig. 3g, it is noteworthy that this RuNi/NC || RuO<sub>2</sub> electrode pair achieves the chlor-alkali electrolysis at a current density of 10 mA cm<sup>-2</sup> with a low cell voltage of 1.96 V, significantly outperforming the Pt/C || RuO<sub>2</sub> combination which requires 2.27 V under identical conditions. Notably, this cell voltage represents by far the



lowest reported for chlor-alkali electrolysis (Supplementary Table 8). Moreover, the authenticity of the anodic CIER is confirmed by iodometric analysis, and rotating ring-disk electrode (RRDE) studies demonstrate an average CIER selectivity exceeding 90% at 1.9 V vs. RHE (Supplementary Figs. 33 and 34). Furthermore, durability tests show that the RuNi/NC || RuO<sub>2</sub> system maintained stable performance during continuous operation at 10 mA cm<sup>2</sup> for 120 h, with minimal voltage fluctuations, highlighting the robustness of RuNi/NC against brine-induced corrosion (Fig. 3h). These performances position RuNi/NC as a promising candidate for large-scale chlor-alkali

electrolysis and other electrochemical processes requiring sustained HER catalysts.

### Mechanic understanding of the tip-intensified HER activity

To study how local interfacial structural manipulation benefits the catalytic activity, we conducted COMSOL Multiphysics finite element simulations to understand the relationship between nanopip curvature and cation concentration at the electrode-electrolyte interface<sup>42–45</sup>. Figure 4a illustrates the increase in electron density at the tip as curvature increases, resulting in a localized enhancement of the

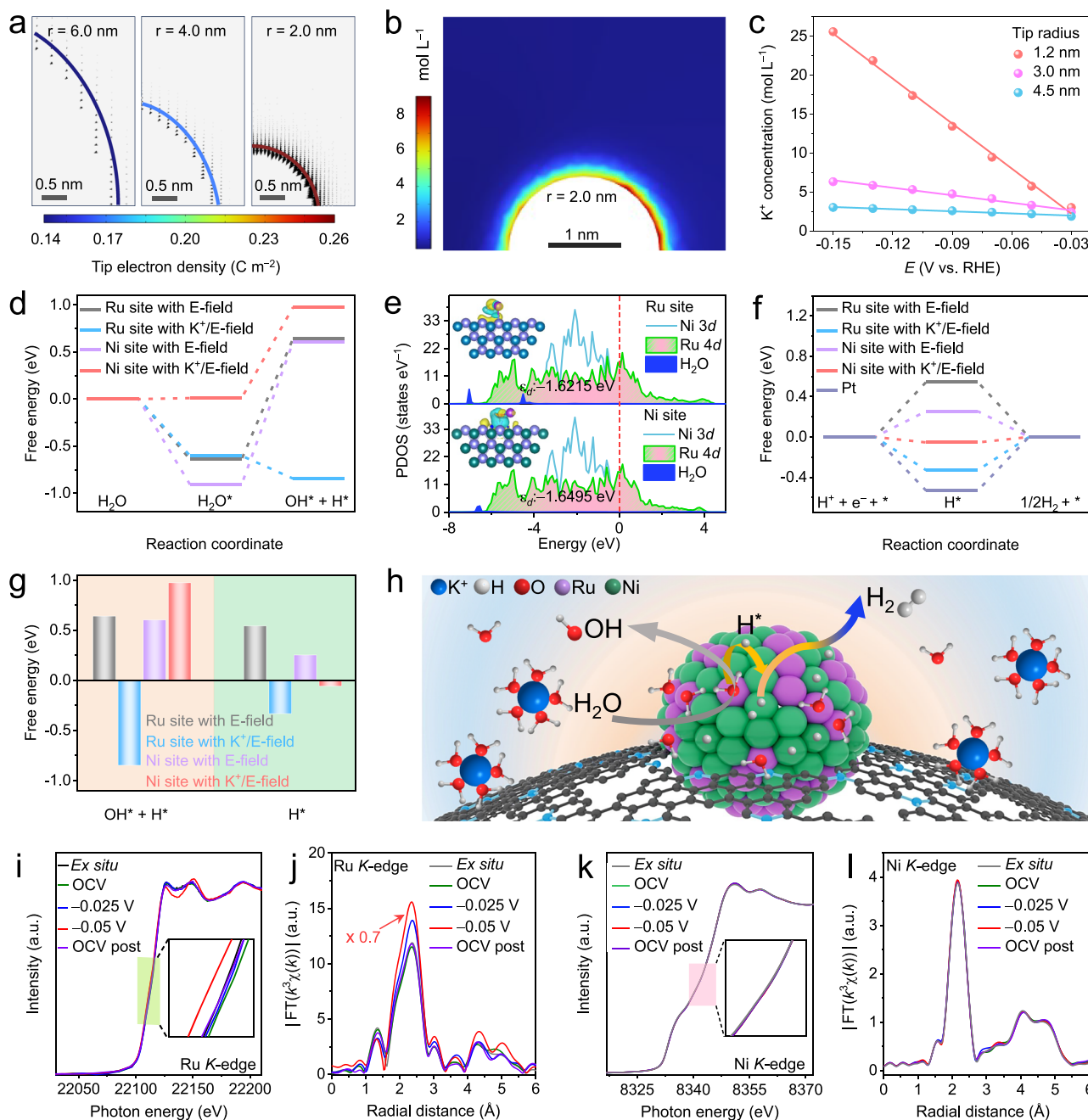


**Fig. 4 | Finite element simulation, DFT calculations and in situ synchrotron X-ray absorption spectroscopic study. a** Color maps of electron density distribution on the surfaces of electrodes with different curvature radii of 2, 4, and 6 nm. **b** Simulated surface density distribution of K<sup>+</sup> on a tip electrode with a curvature radius of 2 nm. **c** The applied potential-dependent local K<sup>+</sup> concentration on different curved tips. **d** Free energy diagrams of H<sub>2</sub>O adsorption/dissociation on different sites without K<sup>+</sup> (denoted as E-field) and with K<sup>+</sup> (denoted as K<sup>+</sup>/E-field).

**e** PDOS of Ru and Ni sites with K<sup>+</sup> on RuNi/NC surface toward H<sub>2</sub>O adsorption. **f** Free energy diagrams of H<sup>+</sup> adsorption on different sites without K<sup>+</sup> (denoted as E-field) and with K<sup>+</sup> (denoted as K<sup>+</sup>/E-field). **g** Comparison of H<sub>2</sub>O dissociation and H<sup>+</sup> adsorption free energies on different sites. **h** Schematic illustration of the proposed HER catalytic mechanism on RuNi/NC. **i** XANES and **j** EXAFS spectra at the Ru K-edge, and **k** XANES and **l** EXAFS spectra at the Ni K-edge of RuNi/NC recorded at different applied voltages during electrocatalytic HER process.

electrostatic field. Quantitative analysis show that reducing the curvature radius from 10 to 1 nm leads to a nearly four-fold increase in the local electric field strength of the electrical double layer (EDL), from  $0.67 \times 10^5 - 2.6 \times 10^5 \text{ kV m}^{-1}$  at  $-0.1 \text{ V}_{\text{RHE}}$  (Supplementary Fig. 35a). This enhancement in electric field strength suggests a significant concentration of hydrated  $\text{K}^+$  cations in the outer Helmholtz layer within the EDL. Applying the Gouy-Chapman-Stern model, we find that a tip with a 2 nm curvature radius exhibits approximately double the surface  $\text{K}^+$  concentration compared to a tip with a 4 nm radius (Fig. 4b and Supplementary Fig. 35b–d). Interestingly, our simulations indicate that tip curvature has a more substantial effect on surface  $\text{K}^+$  concentration than the applied potential (Fig. 4c). These findings support the hypothesis that the tip effect might be leveraged in catalyst design to disrupt the interfacial hydrogen bonding network by inducing  $\text{K}^+$  enrichment within the EDL. This approach may facilitate the release of trapped  $\text{OH}^*$  intermediates, thereby enhancing HER activity<sup>46</sup>.

To delve deeper into the potential influence of concentrated interfacial  $\text{K}^+$  cation on regulating the HER elementary steps, including  $\text{H}_2\text{O}$  adsorption/dissociation and  $\text{H}^*$  adsorption/recombination, density functional theory (DFT) calculations were performed. The slabs were modeled based on the hexagonal RuNi (110) surface given its thermodynamically favored stability (Supplementary Data 1, and Supplementary Figs. 36 and 37). In the presence of a local electric field with a magnitude set at  $-1 \text{ V/\AA}^{29,43}$ , two distinct scenarios were constructed: a layer of  $\text{H}_2\text{O}$  molecules without  $\text{K}^+$  (denoted as E-field) and with  $\text{K}^+$  (denoted as  $\text{K}^+/\text{E}$ -field). Subsequently, the intermediate adsorption on both the Ru site and Ni site were compared. The Gibbs free energy change diagram for  $\text{H}_2\text{O}$  adsorption and dissociation reveals that, in the absence of interfacial  $\text{K}^+$ , both Ru and Ni sites could readily adsorb  $\text{H}_2\text{O}$  (Fig. 4d). However, the introduction of  $\text{K}^+$  renders a selectively discouraged  $\text{H}_2\text{O}$  adsorption on the Ni site, while minimally affecting the Ru site, implying a preference for  $\text{H}_2\text{O}$  adsorption on the oxyphilic Ru site. Notably, a spontaneous  $\text{H}_2\text{O}$  dissociation only on the Ru site is simulated in the presence of interfacial  $\text{K}^+$ , suggesting the pivotal role of interfacial hydrated  $\text{K}^+$  in promoting  $\text{H}_2\text{O}$  dissociation and thus accelerating HER kinetics. The strong  $\text{H}_2\text{O}$  adsorption/dissociation capability on the Ru site is further evidenced by the computed partial density of states (PDOS) of  $\text{H}_2\text{O}$  adsorption with  $\text{K}^+$  and E-field (Fig. 4e), which shows a larger orbit overlap and upshifted d-band center ( $\epsilon_d$ ) on Ru site than that on Ni site. Moreover, Fig. 4f illustrates the Gibbs free energy of  $\text{H}^*$  adsorption ( $\Delta G_{\text{H}^*}$ ), where the presence of  $\text{K}^+$  and E-field endows Ni site with an optimally favorable  $\Delta G_{\text{H}^*}$  approaching zero, implying the dissociated  $\text{H}^*$  intermediates may overflow from Ru site to the adjacent Ni site and preferentially absorb on there. This assertion is further supported by the significantly lower activation free energy calculated for  $\text{H}^*$  migration from a Ru site to an adjacent Ni site compared to that towards another adjacent Ru site (Supplementary Fig. 38). To perceive the impact of interfacial  $\text{K}^+$  on regulating the adsorption behavior of intermediates on Ru and Ni sites, Fig. 4g presents the specific Gibbs free energies for both  $\text{H}_2\text{O}$  dissociation and  $\text{H}^*$  adsorption on Ru and Ni sites. By contrastive analysis, we can deduce that, the tip-intensified HER electrocatalysis of RuNi/NC likely proceed through a cooperative relay between neighboring Ru and Ni sites facilitated by hydrated  $\text{K}^+$ . This hypothesized mechanism entails  $\text{H}_2\text{O}$  adsorption and dissociation on Ru site, followed by the migration of dissociated  $\text{H}^*$  and subsequent Tafel-type recombination on Ni site, i.e. an  $\text{H}^*$  spillover-bridged Volmer–Tafel electrocatalytic process, as schematically depicted in Fig. 4h.

To experimentally validate the catalytic mechanism of RuNi/NC and elucidate the specific roles of Ru and Ni sites, in situ XAS measurements were performed under operational HER conditions to scrutinize the local structural evolutions and electronic changes of RuNi/NC (Supplementary Fig. 39). Figure 4i presents the Ru *K*-edge XANES spectra at varying applied potentials, a slight shift of the absorption edge to the higher energy side under open circuit voltage (OCV) as compared to the ex situ spectrum, indicates an increase in the

oxidation state of Ru. This shift is likely due to the adsorption of  $\text{H}_2\text{O}$  or  $\text{OH}^-$  on Ru atoms, causing electron delocalization and partial surface atom rearrangement<sup>47,48</sup>. As the applied potential shifted to  $-0.025$  and  $-0.05 \text{ V}$ , a gradual shift of absorption edge towards lower energy was observed, indicating a reduced oxidation state of Ru subsequent to  $\text{H}_2\text{O}$  dissociation. This shift signifies rapid  $\text{H}_2\text{O}$  dissociation under the reductive conditions of HER, corroborating the efficacy of Ru in  $\text{H}_2\text{O}$  dissociation. Accordingly, the Ru *K*-edge FT-EXAFS spectra exhibited a noticeable increase in the alloying degree as the applied potential decreased (Fig. 4j), and upon returning to OCV, the Ru–Ni coordination peak recovered, suggesting a highly resilient active sites of RuNi/NC for HER. In contrast, the Ni *K*-edge XANES spectra exhibited imperceptible absorption edge shift under different applied potentials (Fig. 4k), and the intensity of the first-shell peak in the FT-EXAFS spectra marginally increased at  $-0.05 \text{ V}$  (Fig. 4l), probably reflecting an increased alloying degree under cathodic potential. This insensitivity in electronic structure change implies that Ni atoms may not participate in the redox process during HER, aligning well with the non-faradaic Tafel process involving the recombination of two  $\text{H}^*$  to generate the  $\text{H}_2$  gas, thus affirming the role of Ni as an  $\text{H}^*$ -adsorption site in HER. The foregoing analysis unequivocally establishes that HER catalysis by RuNi/NC adheres to a relayed Volmer–Tafel mechanism, wherein Ru and Ni respectively facilitate the  $\text{H}_2\text{O}$  dissociation-related Volmer process and  $\text{H}^*$  recombination-related Tafel process, which are bridged by the  $\text{H}^*$  spillover in between.

## Discussion

We have developed a universal synthetic route for architecting Ni-based bimetallic nanoalloys planted on super-hydrophilic and high-curvature carbon nanocages, which feature the pronounced tip effect. Leveraging these intriguing structural merits, we have successfully achieved the cations penetration-induced reorganization of interfacial hydrogen bonding network through an “on-site disruption and near-site compensation” strategy. The exemplary RuNi/NC demonstrates a high performance in HER, characterized by the tip-intensified high mass activity and low Tafel slope, coupled with strong durability. Moreover, its high catalytic capability has been showcased in both alkaline water electrolysis and high-temperature chlor-alkali electrolysis. Finite element simulations in tandem with DFT calculations suggest the pivotal roles of the tip-induced enrichment of surface  $\text{K}^+$  cations in facilitating the  $\text{H}_2\text{O}$  dissociation-associated Volmer step and the  $\text{H}^*$  adsorption-associated Tafel step. Further mechanistic insights garnered through in situ XAS studies disclose that the superior HER activity is attributed to a synergistic relay between Ru and Ni sites via an  $\text{H}^*$  spillover-bridged Volmer–Tafel catalytic mechanism. This study not only presents a high-performance alkaline HER electrocatalyst but also offers a microscopic perspective for enhancing water dynamics by meticulous local interfacial structural design of catalysts toward water-involved catalysis and beyond.

## Methods

### Chemicals

All chemicals and solvents used in this study were reagent grade and not further purified. Ethylenediamine tetraacetic acid ( $\text{H}_4\text{EDTA}$ ,  $\text{C}_{10}\text{H}_{16}\text{N}_2\text{O}_8$ ,  $\geq 99.5\%$ ), iron chloride hexahydrate ( $\text{FeCl}_3 \cdot 6\text{H}_2\text{O}$ ,  $\geq 99\%$ ), nickel nitrate hexahydrate ( $\text{Ni}(\text{NO}_3)_2 \cdot 6\text{H}_2\text{O}$ ,  $99\%$ ), zinc chloride ( $\text{ZnCl}_2$ ,  $\geq 98\%$ ), *N,N'*-dimethylformamide (DMF,  $\text{C}_3\text{H}_7\text{NO}$ ,  $\geq 99.5\%$ ), triethylamine ( $\text{C}_6\text{H}_{15}\text{N}$ ,  $\geq 99.5\%$ ), sodium hydroxide ( $\text{NaOH}$ ,  $\geq 96\%$ ), sodium chloride ( $\text{NaCl}$ ,  $\geq 99.5\%$ ), potassium dihydrogen phosphate ( $\text{KH}_2\text{PO}_4$ ,  $\geq 99.5\%$ ), dipotassium hydrogen phosphate ( $\text{K}_2\text{HPO}_4 \cdot 3\text{H}_2\text{O}$ ,  $\geq 99\%$ ), isopropanol ( $\text{C}_3\text{H}_8\text{O}$ ,  $\geq 99\%$ ), sulfuric acid ( $\text{H}_2\text{SO}_4$ ,  $95\% - 98\%$ ) and hydrochloric acid ( $\text{HCl}$ ,  $36\% - 38\%$ ) were purchased from Sinopharm Chemical Reagent Co. Ltd. Platinum tetrachloride ( $\text{PtCl}_4$ ,  $99\%$ ) was purchased from Shanghai Haohong Scientific Co. Ltd. Palladium chloride ( $\text{PdCl}_2$ ,  $99\%$ ) was purchased from Shanghai Adamas Reagent Co. Ltd.



Cupric chloride ( $\text{CuCl}_2$ , 98%) was purchased from Aladdin. Potassium hydroxide (KOH, 95%) was purchased from Macklin. Ruthenium chloride hydrate ( $\text{RuCl}_3 \cdot x\text{H}_2\text{O}$ , 99.9%) was purchased from J&K Scientific. Nafion 117 solution was purchased from Dupont. And ultrapure water (18.25 M $\Omega$  cm) from a water purifier system was used in all experiments.

### Synthesis of $[\text{Ni}_2(\text{EDTA})]_n$

A solution was prepared by dissolving 3.32 g (11 mmol) of  $\text{Ni}(\text{NO}_3)_2 \cdot 6\text{H}_2\text{O}$  in 40 mL of DMF, followed by the addition of 3 mL (21.6 mmol) of triethylamine and 1.18 g (4 mmol) of  $\text{H}_4\text{EDTA}$  dissolved in 60 mL of DMF. The resulting mixture was stirred for 1 h to form a precipitate, which was subsequently washed three times with DMF by centrifugation. After drying under vacuum at 60 °C overnight, an aquamarine powder of 2.06 g was obtained.

### Synthesis of Ni@NC

2 g of  $[\text{Ni}_2(\text{EDTA})]_n$  was finely ground and placed in a tube furnace for pyrolysis. It was heated under an Ar atmosphere at a rate of 5 °C min<sup>-1</sup> until reaching 1000 °C, followed by dwelling at this temperature for 1 h. After naturally cooling, a black powder (552.8 mg) was obtained. This powder was then dispersed in a mixed solution of 1 M  $\text{FeCl}_3 \cdot 6\text{H}_2\text{O}$  (28 mL) and 1 M HCl (22 mL) at 80 °C and stirred for 12 h. After cooling, the precipitated solid was washed with ultrapure water several times until a near-neutral centrifugate was achieved. Finally, it underwent vacuum drying at 60 °C overnight to yield a black powder product (171.3 mg).

### General synthesis of MNi/NC (M = Ru, Pt, Pd, Cu, Zn)

The MNi/NC synthesis adheres to a standardized procedure. To begin, 30 mg of Ni@NC and a certain amount of the second metal salts were combined in 20 mL of distilled water and stirred overnight. Then the resulting mixture underwent drying in an oven at 80 °C for 10 h. The ensuing dried powder was subjected to calcination in a tube furnace under an Ar atmosphere enriched with 5%  $\text{H}_2$ . The heating process proceeded at a rate of 5 °C min<sup>-1</sup> to a target temperature and was maintained at this temperature for 2 h, followed by natural cooling to yield the final black powder product. The specific amounts of the second metal salts, calcination temperatures (*T*), and product yields of MNi/NC sample series are as follows, RuNi/NC ( $\text{RuCl}_3 \cdot x\text{H}_2\text{O}$ : 5 mg, *T*: 1000 °C, yield: 21.3 mg), PtNi/NC ( $\text{PtCl}_4$ : 5 mg, *T*: 1000 °C, yield: 22.5 mg), PdNi/NC ( $\text{PdCl}_2$ : 2 mg, *T*: 1000 °C, yield: 23.4 mg), CuNi/NC ( $\text{CuCl}_2$ : 5 mg, *T*: 900 °C, yield: 25.6 mg), ZnNi/NC ( $\text{ZnCl}_2$ : 5 mg, *T*: 600 °C, yield: 22.3 mg). These adjustments ensure the synthesis of distinct MNi/NC nanoalloys while maintaining the overall consistency of the methodology.

### Synthesis of Ru/NC

24.5 mg of RuNi/NC was added into 20 mL of 5 M HCl solution and stirred at 80 °C for 10 h. After cooling, the resulting solid was washed with ultrapure water several times until a near-neutral centrifugate was achieved, followed by vacuum drying at 60 °C overnight to obtain the black powder product (14.5 mg).

### Characterizations

The powder X-ray diffraction (XRD) patterns were obtained on a Rigaku Miniflex600 X-ray diffractometer equipped with a  $\text{Cu-K}\alpha$  radiation source ( $\lambda = 0.154$  nm). The morphology and structure of nanomaterials were observed on transmission electron microscope (TEM, Talos F200X, ThermoFisher Scientific) which was coupled with energy dispersive X-ray spectroscopy (EDS) with an acceleration voltage of 200 kV. Atomic-resolution high angle annular dark field-scanning transmission electron microscope (HAADF-STEM) images and EDS elemental maps were taken using JEM-ARM300F. Detailed chemical compositions were analyzed by X-ray photoelectron spectroscopy (XPS) on ThermoScientific K-Alpha using a monochromatic

Al  $K\alpha$  X-ray beam (1486.6 eV). All binding energies were calibrated using the C 1s peak (284.8 eV). The *K*-edge X-ray absorption fine structure (XAFS) spectra of Ru and Ni elements were recorded at beamlines BL12B2 (SPRING-8) and TPS 44A of the National Synchrotron Radiation Research Center. Raman spectra were collected on WiTech alpha300R using an incident light from a 532 nm laser.  $\text{N}_2$  adsorption-desorption isotherm and the Brunauer-Emmett-Teller (BET) surface area measurements were measured at 77 K using Micromeritics ASAP 2460 instrument. The content of each metal element in the catalysts was determined by inductively coupled plasma atomic emission spectroscopy (ICP-AES) on Intrepid II XSP instrument, while the content of each nonmetal element (EA) in the catalysts was measured by elemental analysis on Vario MICRO. Contact angles of as-prepared materials were measured with a video-based contact angle instrument (OCA 20, Dataphysics).

### 3D electron tomography

The high-resolution TEM tomography tilt series were collected at 200 kV in a JEOL JEM-F200. The electron micrographs were acquired using a single-axis high-tilt tomography holder from -74° to 68° with a linear tilt step of 5°. At each tilt angle, focusing was done on a neighboring particle to decrease beam damage to the region of interest. The image size was 4096 × 4096 pixels at a pixel size of 0.17 × 0.17 Å<sup>2</sup>. Before tilt series alignment, dead pixels and background for each projection were subtracted, and pixel binning was performed using custom-written MATLAB scripts. The acquired tilt series were first coarsely aligned using cross-correlation, then further aligned (via center of mass alignment) and corrected for the rotation axis using the MATLAB script package<sup>49</sup>. The aligned tilt series were reconstructed using the Fourier-based reconstruction algorithm with 200 iterations<sup>50</sup>. The reconstructed 3D volume was segmented and refined by threshold segmentation and Gaussian filter in MATLAB.

### Electrochemical measurements

All electrochemical measurements were performed at ambient temperature (25 °C) and pressure using a CHI760e workstation (Shanghai Chenhua Co. Ltd.). The working electrode was a glassy carbon rotating disk electrode (RDE) (diameter: 5 mm, area: 0.19625 cm<sup>2</sup>). A saturated calomel electrode (SCE) and graphite rod (diameter: 6 mm) were used as the reference electrode and the counter electrode, respectively. The standard potential of the SCE ( $E^0_{\text{SCE}} = 0.241$  V vs. SHE) was calibrated using cyclic voltammetry (CV) test at a scan rate of 1 mV s<sup>-1</sup> with Pt foil serving as both working and counter electrodes in an  $\text{H}_2$ -sparged 0.5 M  $\text{H}_2\text{SO}_4$  solution, and the benchmark thermodynamic  $\text{H}_2/\text{H}^+$  equilibrium potential was defined by averaging the two inter-conversion point values obtained<sup>51</sup>. The measured potentials versus SCE ( $E_{\text{SCE}}$ ) were then converted to a reversible hydrogen electrode scale ( $E_{\text{RHE}}$ ) according to the Nernst equation with ohmic resistance correction:

$$E_{\text{RHE}} (iR\text{-corrected}) = E_{\text{SCE}} + 0.059 \times \text{pH} + 0.241 - iR \quad (1)$$

where *i* is the measured current (A), and *R* is the electrolyte solution resistance ( $\Omega$ ) obtained by electrochemical impedance spectroscopy (EIS), which were recorded at -0.005 V vs. RHE without *iR* compensation in the frequency range of 10<sup>-1</sup> – 10<sup>6</sup> Hz with an amplitude of 5 mV, the value of *R* can be determined from the high-frequency intercept of the Nyquist plot with the real axis (*Z'*), and the standard deviation was derived from at least three independent measurements. The determined practical electrolyte *pH* values are 0.33 ± 0.03 for a 0.5 M  $\text{H}_2\text{SO}_4$  solution, 7.02 ± 0.02 for a 1 M PBS solution, and 13.74 ± 0.12 for a 1 M KOH solution.

To prepare the catalyst slurry for testing, 2 mg of the catalyst was dispersed in a mixed solution containing isopropyl alcohol (655  $\mu\text{L}$ ), ultrapure water (325  $\mu\text{L}$ ) and 5% Nafion solution (20  $\mu\text{L}$ ), and then ultrasonicated for 1 h to achieve uniformity. Next, 24.8  $\mu\text{L}$  of the slurry

was carefully deposited onto the surface of RDE electrode with a pipette gun, resulting a catalyst loading of  $0.25 \text{ mg cm}^{-2}$ . Prior to HER test, Ar was bubbled into the aqueous electrolyte for about 30 min. After a continuous CV activation at a scan rate of  $10 \text{ mV s}^{-1}$  until stabilized current signals were achieved, the linear sweep voltammetry (LSV) was performed at a scan rate of  $5 \text{ mV s}^{-1}$  with a rotation rate of 1600 rpm, and was recorded until three repeated curves were obtained to ensure the accuracy of the electrochemical tests. This repeatable LSV curve was then subject to a background current subtraction for subsequent data process and analysis<sup>52</sup>. To measure the electrochemical double-layer capacitance ( $C_{dl}$ ), CVs were recorded within the non-Faradaic potential range at varied scan rates from  $20 - 100 \text{ mV s}^{-1}$ . Chronopotentiometry (CP) technique was used to evaluate the stability of catalysts. Turnover frequency (TOF) of the catalysts was calculated following the equation<sup>53</sup>:

$$\text{TOF (s}^{-1}\text{)} = \frac{j \times S}{n \times F \times N} \text{ (s}^{-1}\text{)} \quad (2)$$

where  $j$  is the current density ( $\text{A cm}^{-2}$ ),  $S$  is the surface area of the electrode ( $\text{cm}^2$ ),  $n$  is the number of electrons involved ( $n = 2$  for HER),  $F$  is Faraday's constant ( $96485.3 \text{ C mol}^{-1}$ ).  $N$  is the number of active sites on the corresponding electrode. For  $N$  calculation, all metal atoms in RuNi/NC loaded on the electrode were considered as active sites. In this case, the calculated value is a lower limit of TOF.

### HER–CIER electrolysis

The  $\text{H}_2$  evolution performance in chlor-alkali electrolysis was evaluated using a double-walled H-type cell, simulating industrial conditions at  $90^\circ\text{C}$  by a heating circulating water bath system<sup>40</sup>. For the anolyte, a supersaturated NaCl solution ( $\text{pH } 7.01 \pm 0.03$ ) was employed to provide an ample chlorine source for sustained CIER. The catholyte comprised an aqueous mixture of  $3 \text{ M NaCl}$  and  $3 \text{ M NaOH}$  ( $\text{pH } 14.12 \pm 0.11$ ) for HER. The electrochemical cell consisted of separate anodic and cathodic compartments, divided by a cation exchange membrane ( $4 \text{ cm}^2$ ) to facilitate  $\text{Na}^+$  transport. The cathode consisted of either RuNi/NC or 20% Pt/C deposited on carbon paper substrate ( $1 \text{ cm}^2$ ). For the anode, commercial  $\text{RuO}_2$ -coated low carbon steel ( $1 \text{ cm}^2$ ) was utilized. All catalysts were loaded at a consistent mass loading of  $0.25 \text{ mg cm}^{-2}$ . The long-term chronopotentiometric (CP) measurement was performed at  $10 \text{ mA cm}^{-2}$  to assess the stability of the catalysts. The cell voltages are reported without  $iR$ -compensation.

### In situ XAFS measurements

For in situ XAFS measurements, a customized plastic (polyetheretherketone, PEEK) electrochemical cell was used. A three-electrode configuration consisting of a sample-coated carbon paper electrode as the working electrode, a Pt wire as the counter electrode, and an Ag/AgCl electrode (in sat. KCl) as the reference electrode was loaded into the cell for electrochemical tests. The cell compartment was filled with  $30 \text{ mL}$  Ar-saturated aqueous  $1 \text{ M KOH}$  solution ( $\text{pH } 13.74 \pm 0.12$ ). Electrochemical experiments were performed using chronoamperometry technique controlled by a potentiostat under ambient conditions; potentials on working electrode were set at open circuit voltage (OCV) and a series of working voltages according to their polarization curves. After each voltage was applied for  $1 \text{ min}$ , in situ XAFS experimental data were collected with three scans per spectrum.

### Computational details

The electronic structure calculations were performed using spin-polarized density functional theory (DFT) as implemented in the Vienna Ab initio Simulation Package (VASP)<sup>54</sup>. The exchange-correlation effects were described using the Perdew-Burke-Ernzerhof (PBE) functional within the generalized gradient approximation (GGA)

framework. Ionic cores were represented by the projector-augmented-wave (PAW) method. For the plane-wave basis set, a kinetic energy cutoff of  $600 \text{ eV}$  was employed. The Brillouin zone was sampled using a  $5 \times 5 \times 1$  Monkhorst-Pack  $k$ -point mesh for structural optimizations and electronic calculations. Geometric relaxations were performed using the conjugate gradient (CG) algorithm until the energy difference between successive steps was  $<10^{-6} \text{ eV/atom}$  and the maximum force on any atom was below  $0.02 \text{ eV/\AA}$ . To account for van der Waals interactions between the substrate and adsorbates, Grimme's DFT-D3 semi-empirical correction was applied. A vacuum region of  $20 \text{ \AA}$  along the  $z$ -axis was introduced to minimize interactions between periodic images. For a more accurate description of the electronic structure, density of states and  $d$ -band center calculations utilized a denser  $11 \times 11 \times 1$   $k$ -point grid. The computational hydrogen electrode (CHE) model was employed to calculate reaction free energies ( $\Delta G$ ) for the hydrogen evolution reaction (HER). In this approach, the chemical potential of a proton–electron pair ( $\text{H}^+ + \text{e}^-$ ) is equated to that of half a hydrogen molecule ( $1/2\text{H}_2$ ) in the gas phase. The free energy change for each reaction step was computed using the following equation:

$$\Delta G = \Delta E - T\Delta S + \Delta \text{ZPE} - |e|U \quad (3)$$

where  $\Delta E$  represents the reaction energy obtained from DFT calculations,  $T\Delta S$  is the entropic contribution,  $\Delta \text{ZPE}$  is the change in zero-point energy, and  $U$  denotes the applied electrode potential.

The electric field simulation was performed using the method proposed by Peter E. Blöchl et al. to generate a uniform macroscopic electric field within the supercell without the necessity of adding or removing any charge<sup>55</sup>.

To detail our actual electric field calculations, we include relevant settings from our INCAR file:

LDIPOL = .TRUE.

IDIPOL = 3

EFIELD = -1

In this configuration, the electric field is applied along the  $Z$  direction (as indicated by IDIPOL = 3), and the strength of electric field is supplied in units of  $\text{V/\AA}$  with a value of  $-1$  in EFIELD. Dipole corrections to the potential (LDIPOL = .TRUE.) are enabled to avoid interactions between periodically repeated images of the supercell, ensuring that electrons move along the direction of the electric field.

### COMOSOL Multiphysics simulations

To investigate the electric field distribution and potassium ion ( $\text{K}^+$ ) concentration at the electrode surface, a finite element-based multiphysics simulation approach using COMSOL Multiphysics software was employed<sup>56</sup>. The model integrated both electrostatic and species transport phenomena to elucidate the  $\text{K}^+$  density within the electrical double layer. The electric field ( $\mathbf{E}$ ) was derived from the negative gradient of the electric potential ( $V$ ):

$$\mathbf{E} = -\nabla V \quad (4)$$

The charge density ( $\rho_v$ ) was calculated using Gauss's law for the electric field:

$$\rho_v = \nabla \cdot (\epsilon_0 \epsilon_r \mathbf{E}) \quad (5)$$

where  $\epsilon_0$  represents the vacuum permittivity and  $\epsilon_r$  denotes the relative permittivity of the materials ( $78.3$  for the aqueous electrolyte,  $1$  for both Ru and Ni). Ion concentrations within the electrical double layer were determined using the steady-state Poisson–Nernst–Planck equation:

$$\nabla \cdot \left( -D_i \nabla c_i - \frac{z_i D_i F}{RT} c_i \nabla V \right) = 0 \quad (6)$$

where  $c_i$  represents the concentration of  $K^+$  or  $OH^-$  ions,  $z_i$  is the ion valence,  $F$  is the Faraday constant,  $R$  is the gas constant, and  $T$  is the absolute temperature (298.15 K). The diffusion coefficients ( $D_i$ ) for  $K^+$  and  $OH^-$  in water were set to  $2.14 \times 10^{-9}$  and  $2.71 \times 10^{-9} \text{ m}^2 \text{ s}^{-1}$ , respectively<sup>46</sup>. Two-dimensional asymmetric model was constructed to represent the three-dimensional structure of RuNi/NC. The computational domain was discretized using triangular mesh elements for numerical solutions.

## Data availability

All data within the article and the Supplementary Information that support the findings of this study are available, or from the corresponding author upon request. Source data are provided with this paper.

## References

- Slobodkin, I. et al. Electrochemical and chemical cycle for high-efficiency decoupled water splitting in a near-neutral electrolyte. *Nat. Mater.* **23**, 398–405 (2024).
- Guan, D. et al. Hydrogen society: from present to future. *Energy Environ. Sci.* **16**, 4926–4943 (2023).
- Leow, W. R. et al. Electrified hydrocarbon-to-oxygenates coupled to hydrogen evolution for efficient greenhouse gas mitigation. *Nat. Commun.* **14**, 1954 (2023).
- Zuo, Y. et al. High-performance alkaline water electrolyzers based on Ru-perturbed Cu nanoplatelets cathode. *Nat. Commun.* **14**, 4680 (2023).
- Shah, A. H. et al. The role of alkali metal cations and platinum-surface hydroxyl in the alkaline hydrogen evolution reaction. *Nat. Catal.* **5**, 923–933 (2022).
- Sun, Q. et al. Understanding hydrogen electrocatalysis by probing the hydrogen-bond network of water at the electrified Pt–solution interface. *Nat. Energy* **8**, 859–869 (2023).
- Rebollar, L. et al. Beyond adsorption” descriptors in hydrogen electrocatalysis. *ACS Catal.* **10**, 14747–14762 (2020).
- Kang, Y. et al. Mesoporous multimetallic nanospheres with exposed highly entropic alloy sites. *Nat. Commun.* **14**, 4182 (2023).
- Song, R. et al. Ultrafine nanoporous intermetallic catalysts by high-temperature liquid metal dealloying for electrochemical hydrogen production. *Nat. Commun.* **13**, 5157 (2022).
- Chen, Z. W. et al. Unusual Sabatier principle on high entropy alloy catalysts for hydrogen evolution reactions. *Nat. Commun.* **15**, 359 (2024).
- Shen, L. F. et al. Interfacial structure of water as a new descriptor of the hydrogen evolution reaction. *Angew. Chem. Int. Ed.* **59**, 22397–22402 (2020).
- Chen, C. et al. Local reaction environment in electrocatalysis. *Chem. Soc. Rev.* **53**, 2022–2055 (2024).
- Li, P. et al. Hydrogen bond network connectivity in the electric double layer dominates the kinetic pH effect in hydrogen electrocatalysis on Pt. *Nat. Catal.* **5**, 900–911 (2022).
- Cai, L. et al. Improved interfacial  $H_2O$  supply by surface hydroxyl groups for enhanced alkaline hydrogen evolution. *J. Mater. Chem. A* **5**, 24091–24097 (2017).
- Su, L. et al. Electric-double-layer origin of the kinetic pH effect of hydrogen electrocatalysis revealed by a universal hydroxide adsorption-dependent inflection-point behavior. *J. Am. Chem. Soc.* **145**, 12051–12058 (2023).
- Wen, Q. et al. Engineering a local free water enriched micro-environment for surpassing platinum hydrogen evolution activity. *Angew. Chem. Int. Ed.* **61**, e202206077 (2022).
- McCrum, I. T. & Koper, M. T. M. The role of adsorbed hydroxide in hydrogen evolution reaction kinetics on modified platinum. *Nat. Energy* **5**, 891–899 (2020).
- Wang, M. et al. Interfacial water activation by single-atom Co– $N_3$  sites coupled with encapsulated Co nanocrystals for accelerating electrocatalytic hydrogen evolution. *ACS Catal.* **12**, 10771–10780 (2022).
- Zhang, J. et al. Competitive adsorption: reducing the poisoning effect of adsorbed hydroxyl on Ru single-atom site with  $SnO_2$  for efficient hydrogen evolution. *Angew. Chem. Int. Ed.* **61**, e202209486 (2022).
- Sun, K. et al. Interfacial water engineering boosts neutral water reduction. *Nat. Commun.* **13**, 6260 (2022).
- Zhang, J. et al. OH spectator at IrMo intermetallic narrowing activity gap between alkaline and acidic hydrogen evolution reaction. *Nat. Commun.* **13**, 5497 (2022).
- Yu, J. et al. Interfacial electric field effect on electrochemical carbon dioxide reduction reaction. *Chem. Catal.* **2**, 2229–2252 (2022).
- Guo, W. et al. Accelerating multielectron reduction at  $Cu_xO$  nanograins interfaces with controlled local electric field. *Nat. Commun.* **14**, 7383 (2023).
- Goyal, A. & Koper, M. T. M. The interrelated effect of cations and electrolyte pH on the hydrogen evolution reaction on gold electrodes in alkaline media. *Angew. Chem. Int. Ed.* **60**, 13452–13462 (2021).
- Liu, E. et al. Unifying the hydrogen evolution and oxidation reactions kinetics in base by identifying the catalytic roles of hydroxyl-water-cation adducts. *J. Am. Chem. Soc.* **141**, 3232–3239 (2019).
- Zhao, K. et al. Enhancing hydrogen oxidation and evolution kinetics by tuning the interfacial hydrogen-bonding environment on functionalized platinum surfaces. *Angew. Chem. Int. Ed.* **61**, e202207197 (2022).
- Deng, M. et al. Interfacial water enrichment and reorientation on Pt/C catalysts induced by metal oxides participation for boosting the hydrogen evolution reaction. *J. Phys. Chem. Lett.* **13**, 1069–1076 (2022).
- McCrum, I. T. Cations in alkaline hydrogen electrocatalysis. *Nat. Catal.* **5**, 846–847 (2022).
- Cai, C. et al. Atomically local electric field induced interface water reorientation for alkaline hydrogen evolution reaction. *Angew. Chem. Int. Ed.* **62**, e202300873 (2023).
- Chen, X. et al. Revealing the role of interfacial water and key intermediates at ruthenium surfaces in the alkaline hydrogen evolution reaction. *Nat. Commun.* **14**, 5289 (2023).
- Fan, M. et al. A universal strategy toward ultrasmall hollow nanostructures with remarkable electrochemical performance. *Angew. Chem. Int. Ed.* **59**, 8247–8254 (2020).
- Liu, M. et al. Enhanced electrocatalytic  $CO_2$  reduction via field-induced reagent concentration. *Nature* **537**, 382–386 (2016).
- Li, M. et al. RuNi nanoparticles embedded in N-doped carbon nanofibers as a robust bifunctional catalyst for efficient overall water splitting. *Adv. Sci.* **7**, 1901833 (2019).
- Li, M. et al. Ni strongly coupled with  $Mo_2C$  encapsulated in nitrogen-doped carbon nanofibers as robust bifunctional catalyst for overall water splitting. *Adv. Energy Mater.* **9**, 1803185 (2019).
- Gong, S. et al. O species-decorated graphene shell encapsulating iridium-nickel alloy as an efficient electrocatalyst towards hydrogen evolution reaction. *J. Mater. Chem. A* **7**, 15079–15088 (2019).
- Zhang, X. et al. Developing Ni single-atom sites in carbon nitride for efficient photocatalytic  $H_2O_2$  production. *Nat. Commun.* **14**, 7115 (2023).
- Liu, W. et al. Highly-efficient RuNi single-atom alloy catalysts toward chemoselective hydrogenation of nitroarenes. *Nat. Commun.* **13**, 3188 (2022).
- Wang, Q. et al. Coordination engineering of iridium nanocluster bifunctional electrocatalyst for highly efficient and pH-universal overall water splitting. *Nat. Commun.* **11**, 4246 (2020).



39. Su, P. et al. Exceptional electrochemical HER performance with enhanced electron transfer between Ru nanoparticles and single atoms dispersed on a carbon substrate. *Angew. Chem. Int. Ed.* **60**, 16044–16050 (2021).
40. Zhang, L.-N. et al. Cable-like Ru/WNO@C nanowires for simultaneous high-efficiency hydrogen evolution and low-energy consumption chlor-alkali electrolysis. *Energy Environ. Sci.* **12**, 2569–2580 (2019).
41. Salah, A. et al. Advanced Ru/Ni/WC@NPC multi-interfacial electrocatalyst for efficient sustainable hydrogen and chlor-alkali co-production. *Adv. Energy Mater.* **12**, 2200332 (2022).
42. Xue, F. et al. Nanotip-induced electric field for hydrogen catalysis. *Nano Lett.* **23**, 11827–11834 (2023).
43. Liu, D. et al. Atomically dispersed platinum supported on curved carbon supports for efficient electrocatalytic hydrogen evolution. *Nat. Energy* **4**, 512–518 (2019).
44. Gao, F. Y. et al. High-curvature transition-metal chalcogenide nanostructures with a pronounced proximity effect enable fast and selective CO<sub>2</sub> electroreduction. *Angew. Chem. Int. Ed.* **59**, 8706–8712 (2020).
45. Tian, J. et al. Electric-field assisted in situ hydrolysis of bulk metal-organic frameworks (MOFs) into ultrathin metal oxyhydroxide nanosheets for efficient oxygen evolution. *Angew. Chem. Int. Ed.* **59**, 13101–13108 (2020).
46. Kallikragas, D. T. et al. High temperature diffusion coefficients for O<sub>2</sub>, H<sub>2</sub>, and OH in water, and for pure water. *J. Chem. Eng. Data* **59**, 1964–1969 (2014).
47. Cao, L. et al. Identification of single-atom active sites in carbon-based cobalt catalysts during electrocatalytic hydrogen evolution. *Nat. Catal.* **2**, 134–141 (2018).
48. Pang, B. et al. Laser-assisted high-performance PtRu alloy for pH-universal hydrogen evolution. *Energy Environ. Sci.* **15**, 102–108 (2022).
49. Scott, M. C. et al. Electron tomography at 2.4-ångström resolution. *Nature* **483**, 444–447 (2012).
50. Pryor, A. et al. Genfire: a generalized fourier iterative reconstruction algorithm for high-resolution 3D imaging. *Sci. Rep.* **7**, 10409 (2017).
51. Zeledón, J. et al. Methods-A practical approach to the reversible hydrogen electrode scale. *J. Electrochem. Soc.* **169**, 066505 (2022).
52. Faber, M. S. et al. High-performance electrocatalysis using metallic cobalt pyrite (CoS<sub>2</sub>) micro- and nanostructures. *J. Am. Chem. Soc.* **136**, 10053–10061 (2014).
53. Wang, K. et al. Cu-doped heterointerfaced Ru/RuSe<sub>2</sub> nanosheets with optimized H and H<sub>2</sub>O adsorption boost hydrogen evolution catalysis. *Adv. Mater.* **35**, 2300980 (2023).
54. Hu, H. et al. Ni clusters immobilized on oxygen-rich siloxene nanosheets for efficient electrocatalytic oxygen reduction toward H<sub>2</sub>O<sub>2</sub> synthesis. *Dalton Trans.* **53**, 4823–4832 (2024).
55. Petrilli, H. M. et al. Electric-field-gradient calculations using the projector augmented wave method. *Phys. Rev. B* **57**, 14690–14697 (1998).
56. Gao, L. et al. Engineering a local potassium cation concentrated microenvironment toward the ampere-level current density hydrogen evolution reaction. *Energy Environ. Sci.* **16**, 285–294 (2023).

## Acknowledgements

This work was supported by the National Key Research and Development Program of China (2022YFA1505700, L.H.; 2019YFA0210403, L.Z.), National Natural Science Foundation of China (22205232, L.H.; 22222801, X.W.; 21601187, L.Z.), Talent Plan of Shanghai Branch, Chinese

Academy of Sciences (CASSHB-QNPD-2023-020, L.H.), Natural Science Foundation of Fujian Province (2023J06044, L.H.; 2023J01213, L.Z.), and Fund for Distinguished Young Scholars of FJIRSM (CXZX-2022-JQ06, L.H.). XAFS spectroscopic study on Taiwan beamline BL12B2 at SPring-8 (Japan) and beamline TPS 44A of the National Synchrotron Radiation Research Center (NSRRC) are greatly appreciated. The authors also greatly appreciate support by Transmission Electron Microscope Platform and High-performance Computing Platform of Fujian Science & Technology Innovation Laboratory for Optoelectronic Information of China.

## Author contributions

L.Z. and H.H. contributed equally to this work. L.Z. designed this study, L.Z. and H.H. performed the synthesis, characterizations, electrochemical measurements, data curation and analysis. C.S. conducted the 3D electron tomography and participated in the schematic drawings. D.X. and S.Z. carried out the AC-STEM characterization. Y.X. performed the theoretical simulations. H.T.W., K.H.C. and W.X.L. conducted the in situ XAFS study. Y.C.S. and C.W.P. helped in the ex situ XAFS measurements. L.Z. and H.H. wrote the manuscript, and L.H. and X.W. provided suggestions. L.H. supervised and directed this study. All authors discussed the results and commented on the manuscript.

## Competing interests

The authors declare no competing interests.

## Additional information

**Supplementary information** The online version contains supplementary material available at <https://doi.org/10.1038/s41467-024-51370-1>.

**Correspondence** and requests for materials should be addressed to Lili Han.

**Peer review information** *Nature Communications* thanks Dingsheng Wang, Hong Seok Kang and the other, anonymous, reviewer for their contribution to the peer review of this work. A peer review file is available.

**Reprints and permissions information** is available at <http://www.nature.com/reprints>

**Publisher's note** Springer Nature remains neutral with regard to jurisdictional claims in published maps and institutional affiliations.

**Open Access** This article is licensed under a Creative Commons Attribution-NonCommercial-NoDerivatives 4.0 International License, which permits any non-commercial use, sharing, distribution and reproduction in any medium or format, as long as you give appropriate credit to the original author(s) and the source, provide a link to the Creative Commons licence, and indicate if you modified the licensed material. You do not have permission under this licence to share adapted material derived from this article or parts of it. The images or other third party material in this article are included in the article's Creative Commons licence, unless indicated otherwise in a credit line to the material. If material is not included in the article's Creative Commons licence and your intended use is not permitted by statutory regulation or exceeds the permitted use, you will need to obtain permission directly from the copyright holder. To view a copy of this licence, visit <http://creativecommons.org/licenses/by-nc-nd/4.0/>.

© The Author(s) 2024